



High-temperature corrosion mechanism analysis of 310S alloy in typical MSWI flue gas environment at 460–580 °C

Xiaobo Liu^{1,2} · Yin Duan^{1,2} · Lin Zheng³ · Ling Long^{1,2} · Zeinab Khalid^{1,2} · Qunxing Huang^{1,2} · Xuguang Jiang^{1,2}

Received: 24 January 2023 / Accepted: 14 September 2023 / Published online: 2 November 2023
© The Author(s), under exclusive licence to Springer Nature Japan KK, part of Springer Nature 2023

Abstract

To reveal the high-temperature corrosion mechanism of heating surfaces in the typical flue gas environment in the municipal solid waste incineration (MSWI) system, samples of 310S alloy, a commonly used boiler superheater heating surface material, were deposited with NaCl/50 wt.% K₂SO₄ and exposed to a typical MSWI flue gas atmosphere of 7% O₂ + 600 ppm HCl + 100 ppm SO₂ + N₂ at 460, 510, 550, and 580 °C for 168 h for corrosion test. The macroscopic morphology, corrosion kinetics, phase composition of corrosion products, and the distribution and content of elements in the corrosion section were analyzed. Our results showed that the NaCl/50 wt.% K₂SO₄ salt mixture was an extremely corrosive reagent, and its corrosiveness was enhanced with the increase in temperatures. At 460 °C, the salt mixture did not melt, and the corrosion was induced by the reactions between alkali chlorides and alloy, plus the “active oxidation” catalyzed by chlorine. At 510–580 °C, the salt mixtures were completely melted, considerable metal chlorides and some metal sulfides were detected in corrosion products, and the corrosion was controlled by “electrochemical” reactions within the molten salt, coupled with the “active oxidation”. These findings provide new insights into high-temperature corrosion phenomena in MSWI plants.

Keywords Municipal solid waste incineration · High-temperature corrosion · NaCl/K₂SO₄ · Chlorides · Electrochemistry

Introduction

Waste-to-energy is considered to be an efficient and ecological method of managing waste [1]. Such technologies include thermal conversion (pyrolysis, gasification, and incineration), biological conversion (anaerobic digestion), and landfill [2]. Among them, municipal solid waste incineration (MSWI) technology is the most widely used waste thermal treatment technology because of its well-recognized properties in volume reduction and energy recovery [3–5]. A major obstacle to the improvement of MSWI technology is the severe corrosion of critical heating surfaces such as superheaters or reheaters, which limits the development of

boiler steam temperatures in MSWI plants to higher temperatures [6, 7]. A variety of corrosive substances are contained in the flue gas of MSWI boilers in actual operation. The main corrosive substances produced in the process of MSWI include chlorine- and sulfur-containing salt deposits and corrosive gases, such as O₂, SO₂, HCl, NaCl, K₂SO₄, etc. [8–12]

Among these corrosive species, HCl, whose concentration in MSWI flue gas is 300–900 ppm, is generally considered the main contributor to corrosion in MSWI boilers [13–15]. It has been reported that HCl can be converted into Cl₂ in an oxidizing atmosphere, and Cl₂ can penetrate the scale/matrix interface and react with the metal to generate metal chlorides [16, 17]. The metal chlorides are easy to evaporate and diffuse outside through scales at high temperatures due to their high equilibrium vapor pressure properties. When they diffuse to the areas where a higher O₂ partial pressure is established, they will be oxidized into loose non-protective oxides and release Cl₂. Part of the released Cl₂ will penetrate the scale/matrix interface and attack the metal again [18, 19]. So, a cycle process of “permeation–chlorination–oxidation–release” is formed, resulting in the continuous consumption of metal materials. This process is called “active

✉ Xuguang Jiang
jiangxg@zju.edu.cn

¹ State Key Laboratory of Clean Energy Utilization, Institute for Thermal Power Engineering, Zhejiang University, Hangzhou 310027, Zhejiang, China

² Zhejiang University Qingshanhu Energy Research Center, Linan, Hangzhou 311305, Zhejiang, China

³ Hangzhou Xiaoshan Jinjiang Green Energy Co., Ltd., Xiaoshan, Hangzhou 311200, Zhejiang, China

oxidation” [18]. In contrast, the impact of SO_2 on the heating surface of the MSWI boiler is relatively small because of its low concentration property (3.5–200 ppm in the MSWI flue gas) [20–22]. In our previous study, it was found that the effect of low concentration of SO_2 (50–200 ppm) on corrosion was negligible [13]. Furthermore, the salt deposits on the heating surface are also highly corrosive, the common ones are NaCl and K_2SO_4 [23, 24]. NaCl was reported to be more corrosive than gas-phase substances [14, 22]. It can not only react directly with metals at high temperatures to generate chromate or ferrite to consume metals but also generate Cl_2 to cause active oxidation, and the generated chromate or ferrite can also react with the metal to further consume alloy elements [22, 25]. K_2SO_4 has been reported to be less corrosive than alkali chlorides since it does not react with metals to form chromates or ferrites [26–28].

However, although high-temperature corrosion in MSWI systems has been extensively studied, studies on the corrosion mechanisms of metals in typical MSWI flue gas environments where salt deposits and corrosive atmospheres coexist are still relatively scarce [11, 22, 29]. Previous studies often only focused on the high-temperature corrosion mechanism of heating surface materials under the influence of a single factor. Such as under the influence of a corrosive atmosphere [16, 17, 30] or the influence of salt deposits [31, 32], etc. Therefore, the high-temperature corrosion mechanism of heating surface materials under the coupling influence of multiple corrosive media such as chlorine, sulfur, and alkali metals has not yet been determined.

In this work, the high-temperature corrosion mechanism of heating surface material in a typical MSWI flue gas environment where alkali salt deposits coexist with corrosive gases such as HCl and SO_2 was investigated. 310S alloy, which is an excellent heating surface candidate material widely adopted in MSWI plants, was employed as the research object [22]. In previous studies, high levels of sulfates and chlorides were often detected in the ash deposits on the heating surfaces of MSWI boilers [33, 34], where the mass ratio of alkali sulfates to alkali chlorides was about 1:1 [9]. Therefore, in this work, for the simplification of laboratory research, two salts, NaCl and K_2SO_4 , were used as the representatives of alkali chlorides and alkali sulfates, respectively, which were mixed in a mass ratio of 1:1 and deposited on the surface of the 310S alloy sample to simulate the actual salt deposition environment. Four gases, N_2 , O_2 , HCl, and SO_2 , were used in this study and were configured according to the typical proportions in the actual MSWI flue gas to simulate the corrosive flue gas environment [20, 35–37]. Additionally, the influence of temperature was also considered in this study. As suggested by our earlier research, the selection of temperature was based on the principle of estimating the tube wall temperature as the main steam temperature + 60 °C [13]. Four temperatures of 460, 510, 550, and 580 °C were selected, corresponding to

MSWI plants with main stream temperatures of 400, 450, 485, and 520 °C, respectively. Similar temperatures have also been used in studies by others [38]. In this way, the current research can be conducted at temperatures closer to the heating surface temperatures of operating MSWI boilers, thereby providing practical recommendations.

Experimental

Materials preparation

An austenitic steel 310S alloy plate with the composition listed in Table 1 was pre-machined into bulk samples with dimensions of $10 \times 10 \times 5 \text{ mm}^3$. These samples were ground with 320, 600, 1000, and 1500 grit SiC papers successively, and polished with 0.45 μm alumina powder to obtain mirror-like surfaces. During the polishing process, the edges and corners of the samples were also ground to avoid the loss of corrosion products caused by local stress during the test. Subsequently, the samples were degreased and cleaned in acetone by ultrasonic agitation. Finally, the exact dimensions and mass of the samples were measured by a vernier caliper with an accuracy of 0.02 mm and a Sartorius electronic balance with an accuracy of 0.0001 g, respectively. All prepared samples were stored in absolute ethanol before testing to avoid air contamination or oxidation.

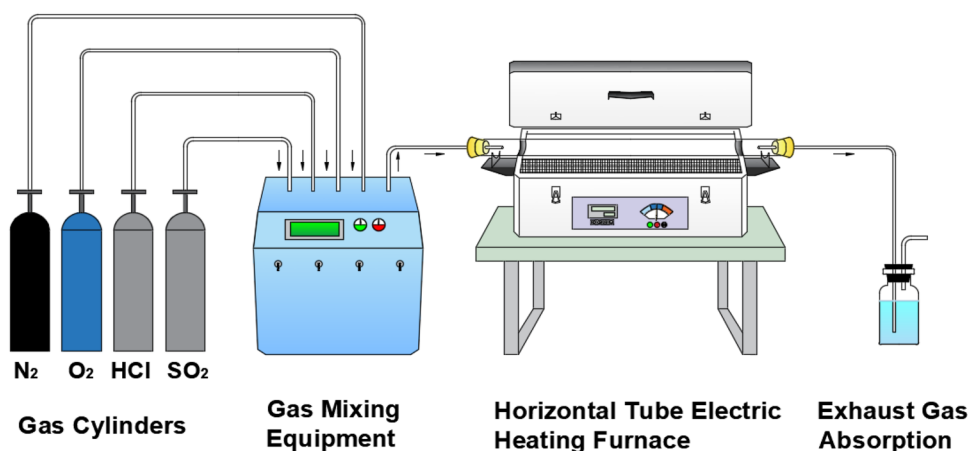
High-temperature corrosion test

High-temperature corrosion tests were performed in a horizontal tube furnace equipped with a gas supply and exhaust gas treatment, as illustrated in Fig. 1. In this study, 310S alloy samples were deposited with NaCl/50 wt.% K_2SO_4 and exposed to an atmosphere of 7% O_2 + 600 ppm HCl + 100 ppm SO_2 + N_2 at 460, 510, 550, and 580 °C for 168 h for corrosion tests. The salt mixture deposits and the complex atmosphere were used to simulate a typical MSWI flue gas environment. The temperatures are selected within the typical temperature range of superheaters in MSWI boilers [39]. The test duration of 168 h was to observe the long-term corrosion behavior of materials, which has been widely adopted in past high-temperature corrosion test studies [19, 39, 40]. The detailed test procedure is as follows:

Before each test, 0.05 g of NaCl and 0.05 g of K_2SO_4 were mixed thoroughly by grinding. Then this 0.1 g of salt powder mixture was evenly deposited on the top surface

Table 1 EDS measured chemical composition (wt. %) of the 310S alloy investigated

Element (wt. %)	Ni	Cr	Mn	Fe
310S	18.83	27.19	1.16	52.82

Fig. 1 High-temperature corrosion test layout

of each sample. The amount of salt deposited was selected based on the range recommended in the ISO 17224:2015 standard. The 0.1 g of deposited salt mixture in this study corresponded to a salt deposition of 25–26 mg/cm² and a salt film thickness of approximately 1.5 mm. Similar salt ratios [41, 42] and amounts of salt deposition [25, 41, 43] have been used in many past studies. As a mixed salt consisting of pure substances, the melting point of the NaCl/50 wt.% K₂SO₄ salt mixture can be found in the previous literature [44], which is ~ 510 °C.

Afterward, each salt-coated sample was placed in an individual porcelain boat, weighed together, and put into the furnace, which was preheated to the desired temperature. The furnace temperature was kept constant throughout the test until the end of the test. The signal for the start of the test was that the exhaust gas absorption device started to bubble after the corrosive gas was introduced. Three parallel samples were used for each test to ensure test accuracy. To obtain the corrosion kinetics data of each sample, the sample was taken out at 24 h, 72 h, and 168 h of exposure. After cooling in air, the sample, the boat, and the exfoliated scales (if any) were weighed together by the Sartorius electronic balance. Then the samples were put back into the furnace to continue the corrosion test until the end of the test. In this way, the mass gain per unit surface area of each sample after corrosion for a certain time can be calculated without affecting the corrosion progress (Eq. 1).

$$\frac{\Delta m}{A} = \frac{m_2 - m_1}{A} \quad (1)$$

Where Δm = the mass gain (mg), m_1 = the initial mass of the sample (mg), m_2 = the mass of the sample after corrosion for a certain time (mg), and A = the sum of six surface areas of the sample (cm²).

Characterization of corrosion products

The cross-section morphologies and element distributions of the corrosion products were investigated by a scanning electron microscope with an energy dispersive X-ray spectrometer (SEM/EDS: Hitachi S-3700N, Tokyo, Japan). The phase composition of the corrosion products was assessed by X-ray diffraction (XRD, Rigaku Rotaflex, Tokyo, Japan) technique with CuK α over the range of 15° < 2 θ < 80°. The procedures required for these characterizations are as follows:

After each corrosion test, the macroscopic morphology of the corroded samples was first photographed. For the 3 parallel samples in each test, different treatments were employed. Specifically, one sample was used for XRD testing, so the corrosion products on its surface were removed with a brush or a tweezer, and then crushed into a fine powder with an agate mortar. Another sample was used to make a cross-section for SEM observation, so this sample was hot-mounted in phenolic resin together with the corrosion products on its surface, and cut with a high-speed cutting machine to obtain a cross-section. The remaining sample was used as a spare. It should be emphasized that the cutting of the samples was carried out under completely dry conditions, which was to avoid the removal of some water-soluble corrosion products. In addition, for the corrosion samples obtained at 460 °C, the unreacted salts on the surface of the samples were removed before mounting to ensure a tight and firm mounting. The cleaning agent and lubricant used in the process of polishing and cleaning the cross-sections of the samples were absolute ethanol, which was also to avoid the dissolution of some water-soluble corrosion products.

Thermodynamic analysis

HSC Chemistry 9.1.1 software (Outotec) was used for thermodynamic equilibrium calculations.

Results

Macroscopic morphology

Figure 2 exhibits the macroscopic morphologies of 310S samples after corrosion tests at different temperatures. At 460 °C (Fig. 2a), in addition to the disappearance of a small amount of salt at the edge of the sample surface, most of the white unreacted salt remained on the sample surface, indicating the salt mixture was difficult to melt at this temperature. In the salt-free area of the sample surface, cracked products existed, showing a loose morphology. At 510 °C (Fig. 2b), no salt was observed on the surface of the sample, instead a complete scale. There were black contaminants in the porcelain boat, which were likely to be the residues of molten liquid salt on the inner wall of the porcelain boat. At 550 °C (Fig. 2c), a complete scale was also formed on the surface of the sample, but there were a few black particles on the scale. Black molten salt contamination in the porcelain boat was also observed, and its contamination area was larger than that at 510 °C. At 580 °C (Fig. 2d), a rough scale was formed on the surface of the sample, and there were small black nodules like coke on the film, implying that

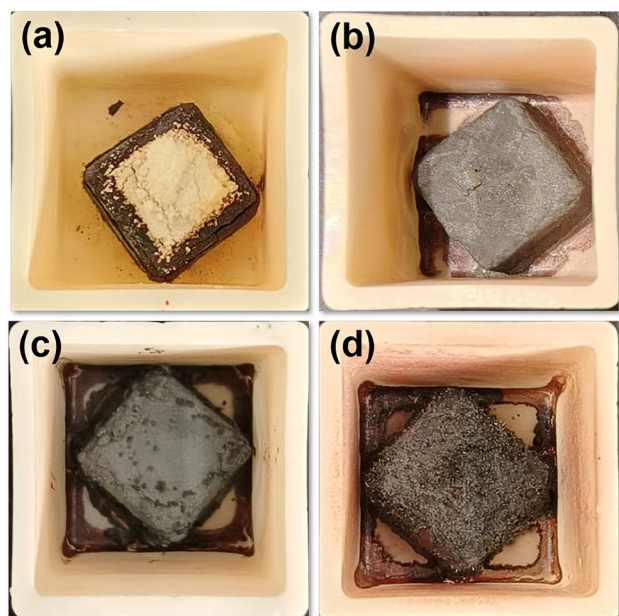


Fig. 2 Macroscopic morphologies of 310S samples after corrosion tests conducted at (a) 460, (b) 510, (c) 545, and (d) 580 °C for 168 h

catastrophic corrosion occurred. The interior of the porcelain boat, including the bottom and the surrounding inner walls, was stained with reddish-brown substances, indicating that the substance may contain iron oxide. These results showed that as the temperature increased from 460 °C to 580 °C, the NaCl/50 wt.% K₂SO₄ salt deposit was transformed from a non-melting state to a completely molten state, and the corrosion attack became more and more serious.

Corrosion kinetics

Figure 3 displays the mass change curves of the 310S alloy exposed at 460–580 °C. From these curves, the corrosion progress of the samples and the evaporation of molten salts can be revealed. As clarified in Fig. 3, with the increase in temperature, the corrosion rate of 310S increased significantly. At 460 °C, the kinetic curve of 310S was parabolic, suggesting that the corrosion process was controlled by diffusion of the gas phase in the scales. The mass change curve of 310S at 460 °C was the lowest position among all the curves, indicating that the corrosion degree of 310S was relatively light when the mixed salt was not melted. Raising the temperature to 510 °C, the position of the curve was elevated and approached a linear development trend, suggesting that the degree of corrosion attack was intensified after the mixed salt was melted. At 550 °C, the curve position was further elevated. Specifically, from 0 to 72 h, the mass gained rapidly in a linear trend, but after 72 h, the corrosion rate decreased slightly, making the overall curve close to a parabola. This phenomenon implied that at 550 °C the scale on the surface of 310S had a certain protective effect, but it may also be related to the

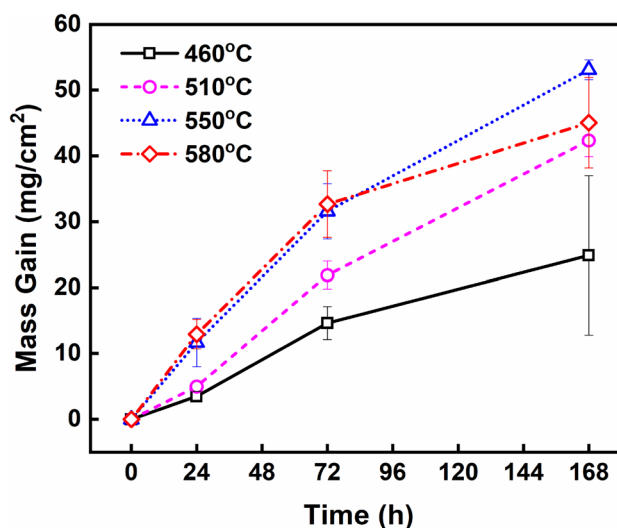


Fig. 3 Mass gain per unit surface area vs exposure time for 310S alloy corroded at different temperatures

reduction of molten salt. At 580 °C, the corrosion rate of 310S did not increase further. The curve almost overlapped with that at 550 °C in the first 72 h, but the slope of the curve dropped sharply after 72 h, and the final mass gain at 168 h was much lower than that at 550 °C. This may be related to the lack of molten salt on the sample surface due to the rapid evaporation of molten salt at 580 °C.

Phase composition of corrosion products

XRD analysis was performed to reveal the phase composition of the corrosion products. Unreacted salts on the sample surface at 460 °C were also examined. As reported in Fig. 4, four compounds including Fe_2O_3 , Cr_2O_3 , Fe_3O_4 , and NaCl were detected in the corrosion products at 460–550 °C, while only two species, Fe_2O_3 and Cr_2O_3 , were found at 580 °C. The absence of Fe_3O_4 at 580 °C indicated that Fe was more fully oxidized at this temperature. It appears that as the temperature increased from 460 °C to 580 °C, the peak intensities of Fe_2O_3 and Cr_2O_3 become more pronounced, in particular, Fe_2O_3 . Consistent with the macroscopic morphological observations (Fig. 2a), distinct NaCl , K_2SO_4 , and KCl peaks were detected in the unreacted salt at 460 °C. The presence of KCl demonstrated that salt reorganization can occur at temperatures close to the melting point of eutectic mixed salts. NaCl was also found in the corrosion products at 510 °C and 550 °C, but its characteristic peak disappeared when the temperature reached 580 °C, suggesting that the evaporation of salts was more vigorous at 580 °C.

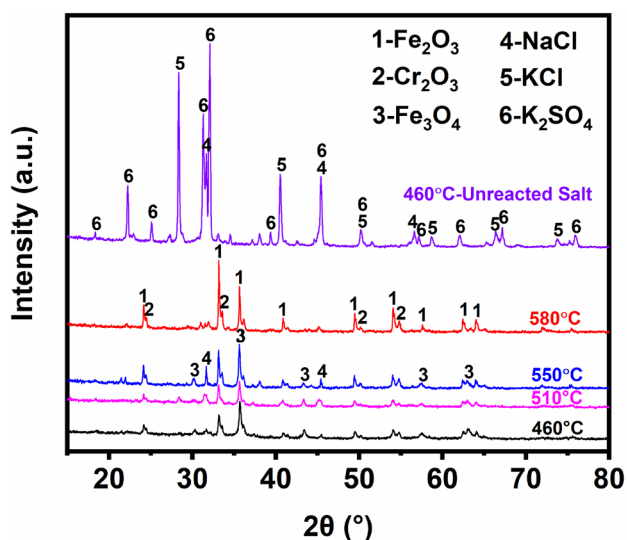


Fig. 4 XRD patterns of corrosion products on the surfaces of 310S alloy corroded at different temperatures

Elemental distribution on cross-section

EDS elemental mapping was conducted to clarify the detailed distribution of different corrosion products on the sample cross-section. Figures 5, 6, 7 and 8 show the cross-sectional element distribution results of 310S alloy samples corroded at 460, 510, 550, and 580 °C for 168 h, respectively.

As is obvious in Fig. 5, at 460 °C, O, Cr, and Fe were the main elements distributed in corrosion products. Compared with Cr, Fe was more enriched in external corrosion products, confirming the abundant presence of Fe_2O_3 or Fe_3O_4 . The simultaneous presence of Cr and O in the internal corrosion products indicated the presence of Cr_2O_3 . The elements of S, Cl, K, and Na in the entire corrosion products were relatively less, indicating that these oxide scales had a certain blocking effect on Cl and S. The distribution positions of S and K were generally consistent, which could be determined to be K_2SO_4 . The distribution position of Cl overlapped more with that of Cr and Na, implying the possible existence of NaCl and CrCl_2 in the internal corrosion products. Besides, almost no Ni element was detected in the corrosion products, implying the preferential oxidation of Fe and Cr.

As presented in Fig. 6, at 510 °C, O, Fe, and Cr were still the primary elements in the corrosion products. Similar to that at 460 °C, Cr_2O_3 was the dominant specie in the internal corrosion products, and Fe_2O_3 or Fe_3O_4 was the dominant specie in the external corrosion products. A new finding was that an obvious Ni-rich band appeared at the edge of the matrix, which demonstrated that Fe and Cr in the matrix were selectively corroded, leaving solely Ni in metallic form. This phenomenon has also been reported previously [38, 45]. Specifically, at the positions corresponding to several Cl-rich groups at the edge of the matrix, except for Cr, these positions were replaced by black dots on the Fe and Ni maps. Furthermore, the distribution positions of Cr and Cl in the internal corrosion products near the matrix were also consistent. Therefore, it is inferred that the main species at the edge of the matrix should be CrCl_2 , in other words, Cr in the metal matrix was preferentially chlorinated. S was relatively enriched in the corrosion products near the substrate/corrosion product interface, and the only other element enriched there was Cr, so it is inferred that S at this location may be in the form of a Cr sulfide. Several overlaps of Cl and Na were observed in the outer region of the corrosion products, which should be the residual NaCl on the sample surface. Compared with 460 °C, the enrichment of Cl at the corrosion products and the edge of the matrix became more remarked at 510 °C, suggesting that the penetration mode of Cl may have changed.

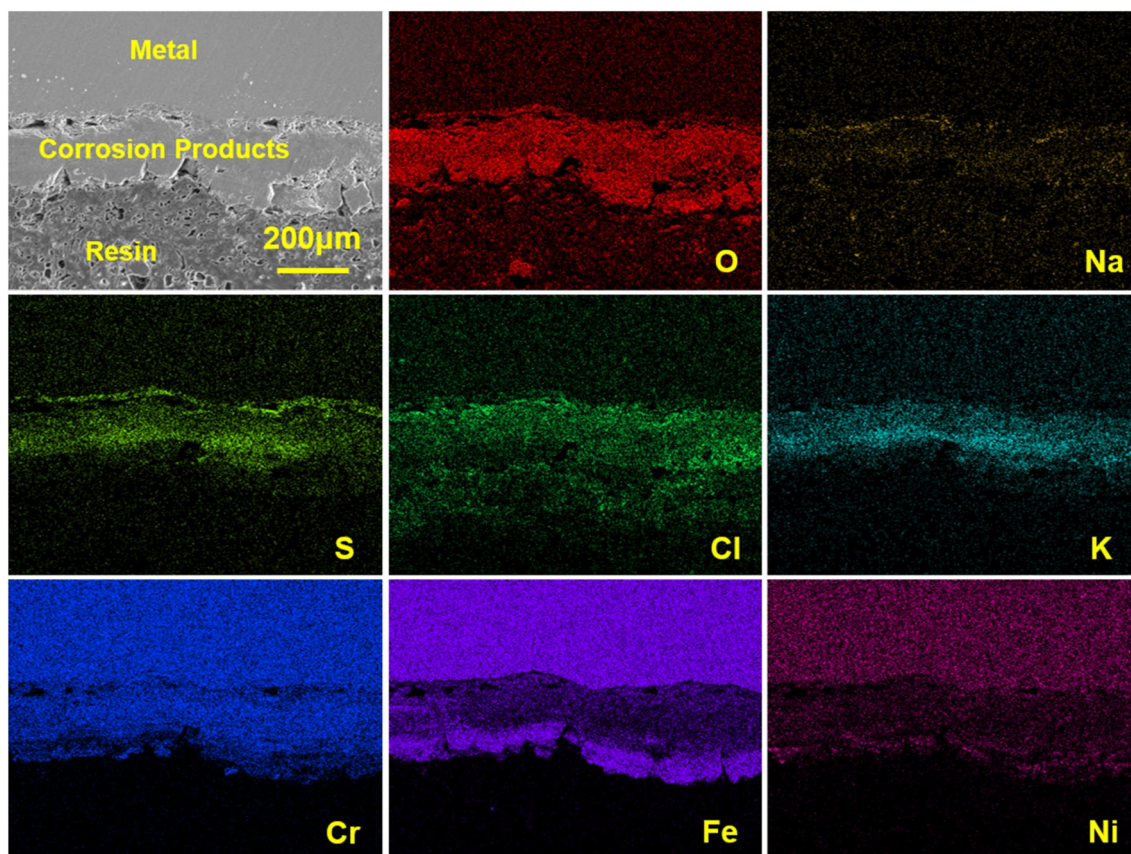


Fig. 5 EDS element map of the cross-section of the 310S alloy sample after corrosion at 460 °C for 168 h

As the temperature increased further to 550 °C (Fig. 7), the distribution positions of Cr, Fe, and Ni were also similar to those at 510 °C, that is, the external corrosion products were dominated by Fe_2O_3 or Fe_3O_4 , the internal corrosion products were dominated by Cr_2O_3 , and the edge of the matrix was enriched with metallic Ni. Unlike at 460 and 510 °C, the Cl element was no longer distributed over the entire cross-section of the corrosion products but occurred in the corrosion products closer to the matrix/scale interface, where the distribution points of Cl and Cr elements coincided, implying the existence of CrCl_2 . Regarding the Cl-enriched region displayed at the edge of the matrix, considering that its distribution shape was round and divergent, it should not be the penetration of Cl in the matrix, but the chloride contamination overflowing from the cracks at the matrix/scale interface. In addition, there is a region in the corrosion product near the surface of the substrate where S is particularly enriched, and the only other element that coincides with this location is Cr. This phenomenon reconfirms that sulfides of Cr are generated when molten sulfate occurs at temperatures higher than 510 °C.

As can be seen in Fig. 8, after the temperature reached 580 °C, Na, K, and S elements almost disappeared in the

corrosion products. This demonstrates faster evaporation of molten salt at this temperature. The distribution positions of Fe, Cr, and Ni elements were the same as those at 510 and 550 °C. Likewise, selective corrosion was observed. Ni was markedly enriched at the edge of the matrix in a metallic state, Cr was enriched in the internal corrosion products in the form of Cr_2O_3 , and Fe existed in the external corrosion products in the form of Fe_2O_3 . What's more, at the metal matrix edge where Cl was present, a distinct Cr-depleted region was observed, while where Fe and Ni were still abundant. This result indicated that the chlorination of Cr was more preferential and faster than that of Fe and Ni at the higher temperature of 580 °C. Correspondingly, Cr-rich oxides were formed near the edge of the metal matrix. In addition, it is worth mentioning that the intrusion process of Cl was vividly displayed at 580 °C. As detailed in Fig. 8, Cl elements were distributed in two-layer regions on the cross-section, that is, the corrosion products and the edge of the matrix. The corrosion products containing relatively more Cl have been separated from the matrix, and the edge of the matrix containing less Cl was also about to fall off since some pores appeared between it and the matrix. This

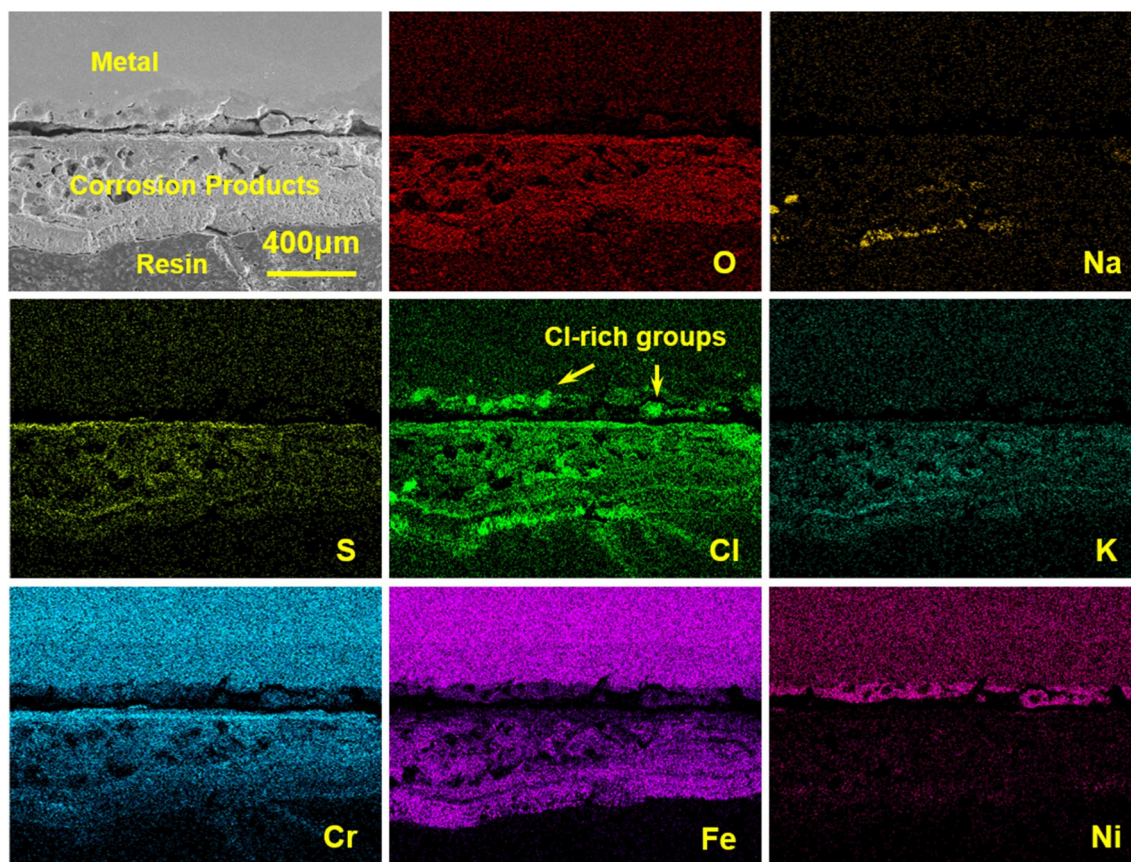


Fig. 6 EDS element map of the cross-section of the 310S alloy sample after corrosion at 510 °C for 168h

phenomenon indicates that the attack of Cl was carried out layer by layer.

Cross-section morphology and composition

To further determine the composition of corrosion products at each temperature, EDS spot scans were carried out and the results are given in Fig. 9. Combined with the results of the preceding qualitative analysis, reasonable compositions at the corresponding locations on the cross-sections were identified, and labeled in Fig. 10.

As observed in Fig. 10a, at 460 °C, a scale of ~200 µm was formed on the surface of the metal matrix. Porosity developed between the scale and the matrix, indicating a tendency for the scale to detach from the matrix. 28.05 wt.% Cr and 33.64 wt.% O elements were detected inside the scale (marked at A₁), verifying the presence of Cr₂O₃. The content of Ni element (6.16 wt.%) and Fe element (10.57 wt.%) was less, which was consistent with the elemental mapping results in Fig. 5. Only 4 wt.% Cl and 6.72 wt.% S elements were detected at point A₁, confirming the protective effect of the scale. On the outer edge of the scale (marked at A₂),

43.97 wt.% Fe and 29.55 wt.% O elements were found, which confirmed the existence of Fe₂O₃. Concerning the large amount of unreacted salt mixture accumulated on the outer surface of the scale observed in Fig. 2a, it was not included in the cross-sectional morphology for the convenience of making the cross-section.

As the temperature increased to 510 °C (Fig. 10b), scales of 300–500 µm were formed on the surface of the sample, and there were obvious continuous cracks between the scales and the matrix. The O content at the edge of the matrix (marked at B₁) was as low as 13.53 wt.%, indicating that most of the metal elements at point B₁ had not been oxidized and still existed in a metallic state. Compared with the initial composition of the alloy, the content of Fe and Cr at point B₁ decreased, and the content of Ni increased. A reasonable explanation was that Fe and Cr were consumed by selective corrosion and diffused out, leaving Ni behind. In addition, 23.56 wt.% of Cl elements existed at point B₁, demonstrating that Cl could penetrate through the outer oxide scales to the substrate surface. Combined with the element distribution results in Fig. 6, it is determined that the substance at point B₁ was CrCl₂. This phenomenon is further addressed thermodynamically in Sect. 4.1. The internal corrosion products

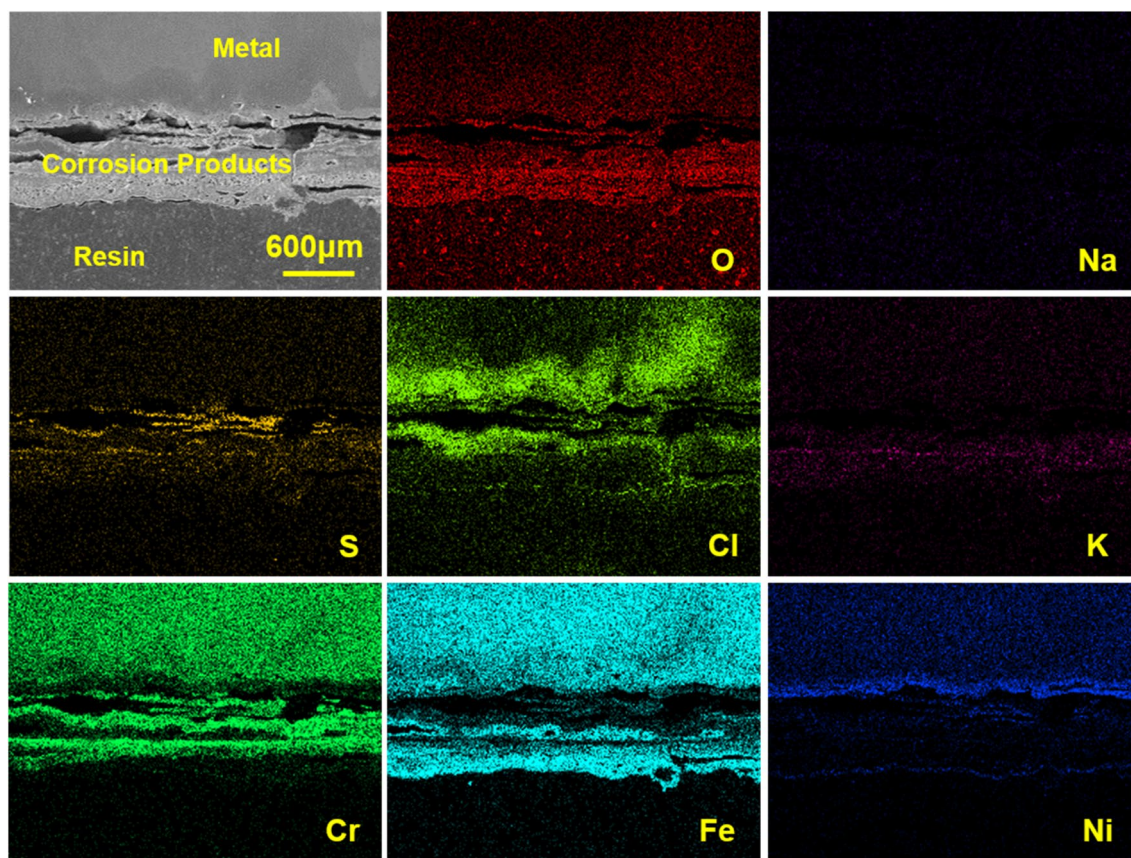


Fig. 7 EDS element map of the cross-section of the 310S alloy sample after corrosion at 550 °C for 168h

contained various elements (marked at B_2), the main substances were identified as Cr_2S_3 , $CrCl_2$, Cr_2O_3 , and Fe_2O_3 . The simultaneous existence of Cr_2S_3 , $CrCl_2$, and Cr_2O_3 indicated that Cr_2O_3 was indeed transformed from Cr_2S_3 and $CrCl_2$. Apart from Fe_2O_3 , considerable NaCl (composed of 11.3 wt.% Na and 24.37 wt.% Cl) remained in the external corrosion product (marked at B_3), which suggested that some salt mixtures had not been completely consumed after the corrosion test at 510 °C for 168 h, which was consistent with the XRD and EDS mapping results (Figs. 4 and 6).

After raising the temperature to 550 °C (Fig. 10c), scales of ~500 μm were formed. The scales were internally stratified, and recognizable (up to 200 μm at the widest) gaps were observed between them and the matrix. There was 49.85 wt.% Fe, 13.24 wt.% Cr, and 29.24 wt.% O in the outer scales (marked at C_1), indicating that the substances at point C_1 were Fe_2O_3 and Cr_2O_3 . The element composition at the matrix/scale interface (marked at C_2) was similar to that at point C_1 , except that 11.28 wt.% Cl occurred at point C_2 , demonstrating the presence of $CrCl_2$ at point C_2 besides Fe_2O_3 and Cr_2O_3 . At a particular location (marked at C_3) near the matrix/scale interface, high levels of the elements Cr (32.38 wt.%) and S (15.92 wt.%) were detected.

In combination with the results of the elemental distributions (Fig. 7), it can be determined that sulfide of Cr (Cr_2S_3 maybe) is predominantly present at point C_3 . This result proves that internal sulfidation occurred during the corrosion process. In addition, at the edge of the matrix (marked at C_4), 72.76 wt.% of Ni was detected, followed by 8.39 wt.% of Fe and 5.57 wt.% of Cr. This shows that the Fe and Cr contents in the matrix were greatly reduced due to selective corrosion, leaving a large amount of Ni. The extremely low O element content (7.54 wt.%) at point C_4 further demonstrated that these Ni existed in a metallic state.

When the temperature was increased to 580 °C (Fig. 10d), the corrosion attack further deteriorated, not only 400 μm scales were formed, but also pores and cracks appeared inside the matrix, which meant that further corrosion attacks had started and were ongoing. The content of Fe and Cr in the matrix (marked at D_1) dropped to 35.14 wt.% and 7.24 wt.%, respectively, while the content of Ni rose to 41.09 wt.%. The content of the O element at point D_1 was extremely low (8.9 wt.%), demonstrating that the alloying elements in the matrix still stayed metallic. These data indicated that selective corrosion also existed at 580 °C. In addition, the internal corrosion products near the matrix/

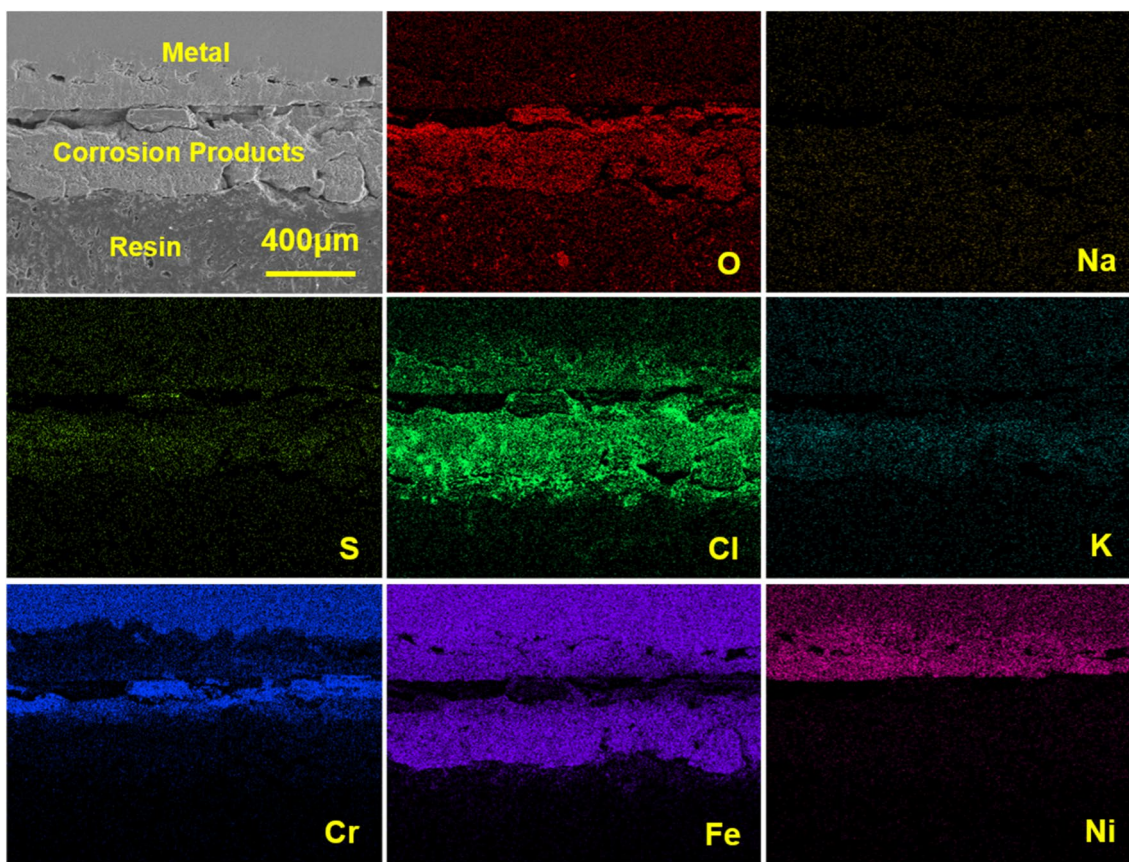


Fig. 8 EDS element map of the cross-section of the 310S alloy sample after corrosion at 580 °C for 168h

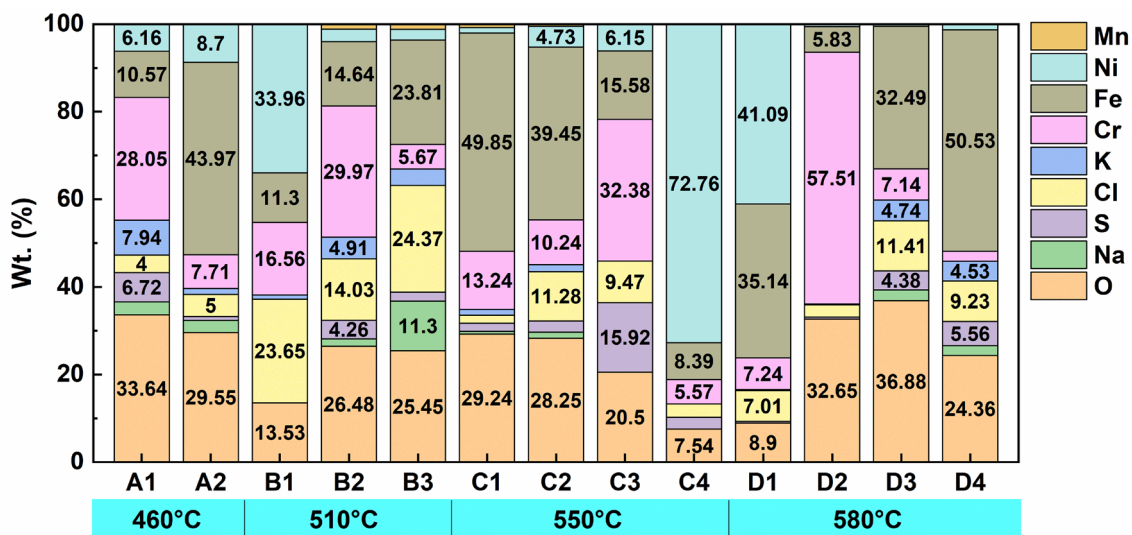
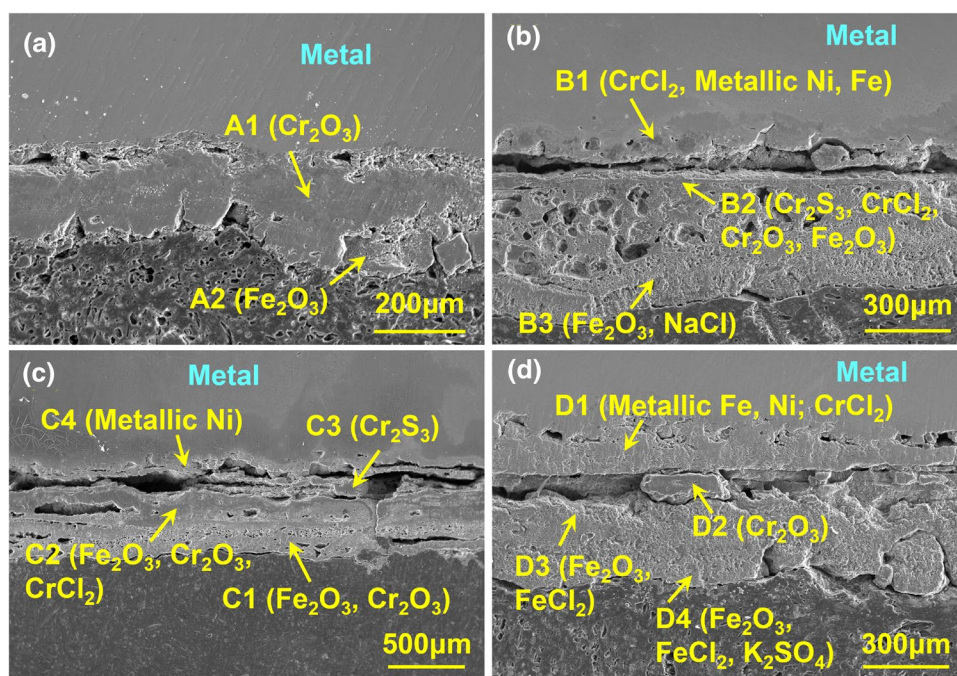


Fig. 9 EDS results (wt. %) of cross-sections of 310S alloy corroded for 168h at different temperatures

scale interface (marked at D₂) were primarily Cr₂O₃. The primary composition of the internal corrosion products at point D₃ was determined to be a large amount of Fe₂O₃ and a

small amount of FeCl₂, as well as possibly a small amount of Cr₂S₃. The main component of the external corrosion

Fig. 10 Cross-sectional morphologies of corrosion products of 310S alloy corroded at different temperatures for 168h: (a) 460 °C, (b) 510 °C, (c) 550 °C and (d) 580 °C



products (marked at D₄) was identified as a significant amount of Fe₂O₃ along with a small amount of FeCl₂ and K₂SO₄.

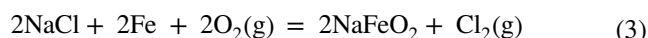
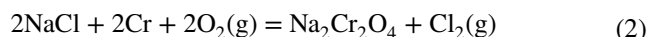
Discussion

In light of the results of the macro-morphologies, corrosion kinetics, phase composition, cross-sectional microstructure, and elemental distribution, the high-temperature corrosion behaviors of 310S alloy samples were very different at various temperatures. In this study, the corrosion was induced by NaCl and K₂SO₄ in the deposited molten salt and HCl, SO₂, and O₂ in the atmosphere. Considering that the melting point of NaCl/50 wt.% K₂SO₄ mixture is around 510 °C [44], the corrosion mechanisms were discussed in two cases (460 °C and 510–580 °C).

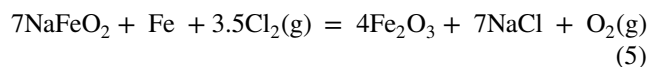
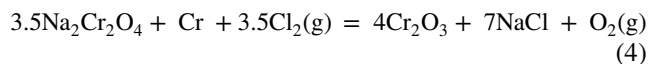
Corrosion mechanism analysis at 460 °C

At 460 °C, only a small part of the NaCl/K₂SO₄ mixed salt melted (seeing Fig. 2a), so it can be considered that the corrosion occurred under the deposition of solid salt powder and in an oxidizing atmosphere containing HCl and SO₂. In this case, the main corrosion reactions involved were gas–solid and solid–solid reactions. Chemical corrosion played a dominant role. Based on the presence of a small amount of Cl inside the corrosion products, a mechanism of “active oxidation” dominated by Cl₂ diffusion is plausible.

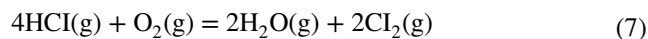
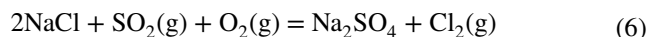
As depicted in Fig. 11, corrosion began with the reaction of NaCl with the metal at the matrix/salt interface to form Na₂CrO₄ or Na₂FeO₄ [22], which consumed the alloy elements and produced Cl₂:



The chromate, ferrite, and Cl₂ released by these reactions would continue to consume the Fe and Cr elements in the matrix and produce porous oxide scales [46]:



At the same time, Cl₂ could be also generated from the reactions between O₂, HCl, and SO₂ in the atmosphere and the salts on the sample surfaces [47, 48]:



When the Cl₂ reached the salt/matrix interface, “active oxidation” occurred. Cl₂ reacted with the alloy to form metal chlorides (FeCl₂, CrCl₂, and NiCl₂, of which Ni has a less reactive behavior [19]) via reaction (6):

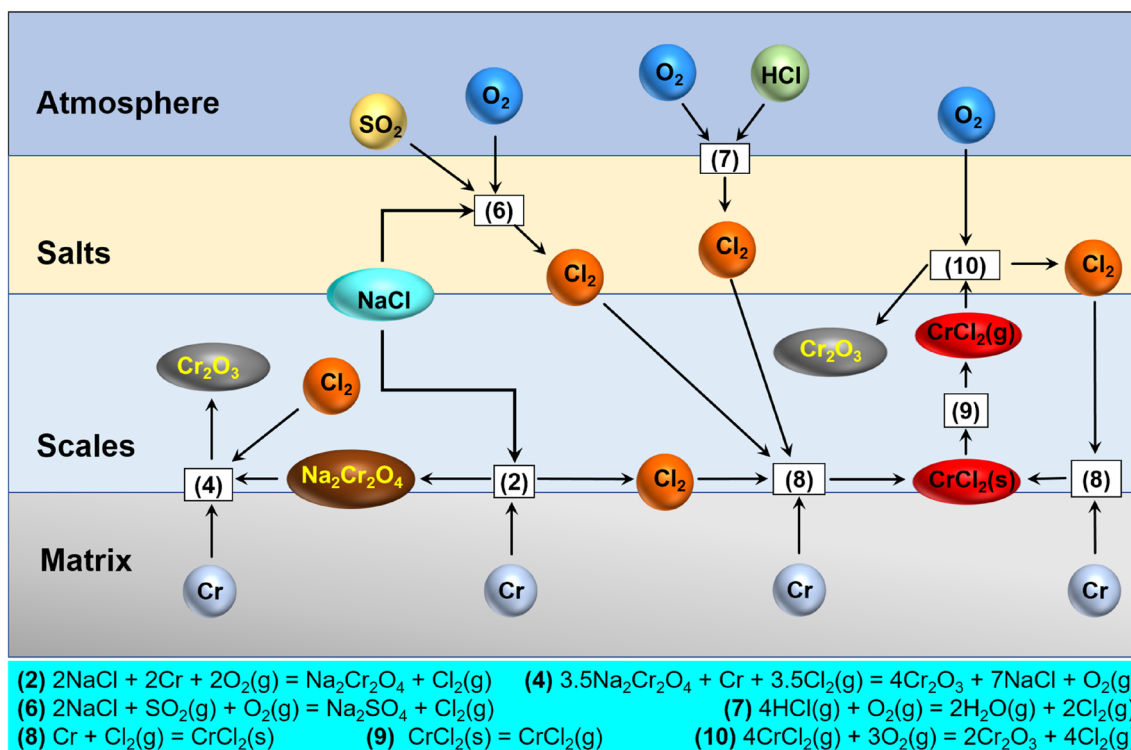
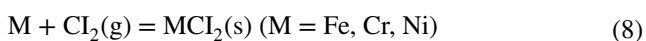


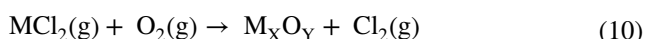
Fig. 11 Schematic diagram of corrosion mechanism of 310S alloy at 460°C (taking Cr as an example)



Then the evaporation of $FeCl_2$, $CrCl_2$, and $NiCl_2$ took place since these metal chlorides have a high vapor pressure:



When they diffused to a place where the O_2 partial pressure was sufficiently high, they were converted to oxides, and Cl_2 was released again:



Therefore, in a short time, loose and porous scales containing Cr_2O_3 , Fe_2O_3 , or Fe_3O_4 were formed on the sample surfaces (seeing Fig. 4), leading to an increase in the mass of the samples. Part of the released Cl_2 could return to the matrix surface and participate in the next attack.

As the corrosion was processed, more metal oxides and chlorides were formed. Then the mixing of the metal chloride and the alkali salt took place, forming a lower melting eutectic salt (e.g., the temperature of the eutectic point of the binary $NaCl-FeCl_2$ system is 370 °C at 58:42 mol fraction) [41]. As a consequence, the mixed salts at the edges of the samples where the temperature was relatively higher melted. Thus, the corrosion rates of the samples further

increased during 24–72 h due to the presence of local molten salts. In the later stage of corrosion, thicker scales formed on the surface of the sample, although they were not dense enough, they still hindered the transportation of the corrosion medium to a certain extent. Therefore, within 72–168 h, the corrosion rate decreased. The reactions mentioned above are all thermodynamically spontaneous, and the Gibbs free energy changes of these reactions at 460, 510, 550, and 580 °C calculated by HSC are shown in Table 2.

For the dislocation morphology of different types of oxide distribution, it has been found that this phenomenon is mainly related to the thermodynamic properties of the metal chlorides. Among $FeCl_2$, $CrCl_2$, and $NiCl_2$, the equilibrium vapor pressure of $CrCl_2$ is the smallest, which can be simply understood as $CrCl_2$ is the third to evaporate among the three [38, 49]. And the O_2 partial pressure required for the conversion of $CrCl_2$ to Cr_2O_3 at the same temperature is also much smaller than that of Fe and Ni [19]. Therefore, these data demonstrate that $CrCl_2$ can only diffuse a short distance before being oxidized. In contrast, $FeCl_2$, which has the highest equilibrium vapor pressure among the three and can only be oxidized at a higher oxygen partial pressure [50], needs to be transported a long distance before it can be converted (Figs. 5, 6, 7, 8).

Table 2 The reactions involved in the proposed corrosion mechanism and their corresponding calculated Gibbs free energy changes (ΔG at 460, 510, 550, and 580 °C) (calculated by HSC Chemistry 9.1.1)

Chemical reactions	ΔG (kJ/mol)			
	460 °C	510 °C	550 °C	580 °C
$2\text{NaCl} + 2\text{Cr} + 2\text{O}_2(\text{g}) = \text{Na}_2\text{Cr}_2\text{O}_4 + \text{Cl}_2(\text{g})$	-653.33	-642.59	-634.01	-627.58
$2\text{NaCl} + 2\text{Fe} + 2\text{O}_2(\text{g}) = 2\text{NaFeO}_2 + \text{Cl}_2(\text{g})$	-418.82	-407.48	-398.32	-391.38
$7\text{Na}_2\text{Cr}_2\text{O}_4 + 2\text{Cr} + 7\text{Cl}_2(\text{g}) = 8\text{Cr}_2\text{O}_3 + 14\text{NaCl} + 2\text{O}_2(\text{g})$	-2969.75	-2943.62	-2922.97	-2907.63
$14\text{NaFeO}_2 + 2\text{Fe} + 7\text{Cl}_2(\text{g}) = 8\text{Fe}_2\text{O}_3 + 14\text{NaCl} + 2\text{O}_2(\text{g})$	-2091.04	-2068.92	-2052.44	-2040.80
$2\text{NaCl} + \text{SO}_2(\text{g}) + \text{O}_2(\text{g}) = \text{Na}_2\text{SO}_4 + \text{Cl}_2(\text{g})$	-109.69	-99.96	-92.22	-86.43
$4\text{HCl}(\text{g}) + \text{O}_2(\text{g}) = 2\text{H}_2\text{O}(\text{g}) + 2\text{Cl}_2(\text{g})$	-18.21	-11.46	-6.05	-1.99
$\text{Ni} + \text{Cl}_2(\text{g}) = \text{NiCl}_2$	-194.13	-186.88	-181.11	-176.80
$\text{Cr} + \text{Cl}_2(\text{g}) = \text{CrCl}_2$	-295.78	-290.04	-285.51	-282.14
$\text{Fe} + \text{Cl}_2(\text{g}) = \text{FeCl}_2$	-248.15	-242.28	-237.61	-234.11
$4\text{FeCl}_2(\text{g}) + 3\text{O}_2(\text{g}) = 2\text{Fe}_2\text{O}_3 + 4\text{Cl}_2(\text{g})$	-547.29	-512.39	-484.70	-464.07
$4\text{CrCl}_2(\text{g}) + 3\text{O}_2(\text{g}) = 2\text{Cr}_2\text{O}_3 + 4\text{Cl}_2(\text{g})$	-1222.00	-1188.30	-1161.45	-1141.38
$2\text{NiCl}_2(\text{g}) + \text{O}_2(\text{g}) = 2\text{NiO} + 2\text{Cl}_2(\text{g})$	-136.83	-124.26	-114.24	-106.75

Corrosion mechanism analysis at 510–580 °C

At 510–580 °C, we found the black pollutants on the inner wall of the porcelain boat, the selective corrosion of Fe, Cr, and Ni at the edge of the matrix, the layered precipitation of more Fe_2O_3 and Cr_2O_3 on the metal surface, and especially the presence of high levels of Cl and low levels of S elements in the corrosion products. From all these indications, a mechanism involving both “electrochemistry” + “active oxidation” is suggested.

At the initial stage of corrosion, the surfaces of the polished samples were free of oxides, so the Fe, Cr, and Ni elements on the alloy surface were directly exposed to the corrosion test conditions provided in this study. Shortly afterward, molten salts were generated on the sample surfaces since the ambient temperature was higher than the melting point of $\text{NaCl}/\text{K}_2\text{SO}_4$. Then, the metallic Fe, Cr, and Ni were dissolved in the $\text{NaCl}/\text{K}_2\text{SO}_4$ melt, and at the same time, O_2 , HCl , and SO_2 in the ambient atmosphere also dissolved into the melt and react with it.

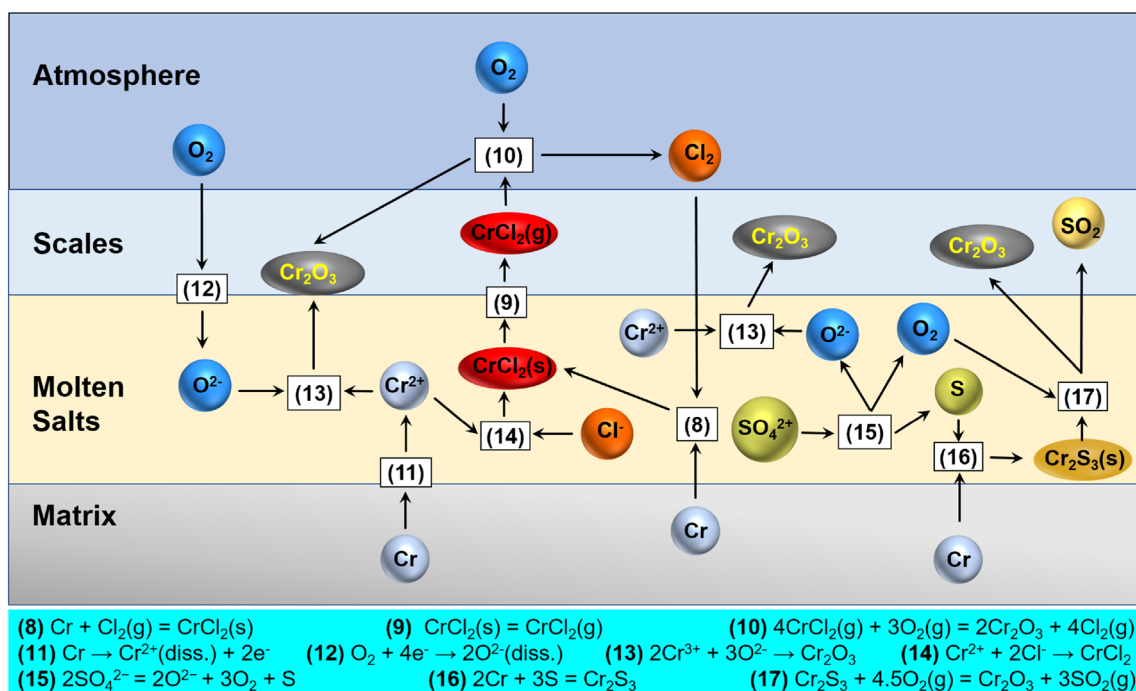
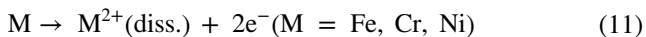


Fig. 12 Schematic diagram of the electrochemical corrosion mechanism of 310S alloy at 510–580 °C (taking Cr as an example)

Because of the limited solubility and diffusion coefficient of oxygen in molten salt, the O_2 partial pressure at the gas phase/melt interface was high, while that at the melt/metal interface was low. Therefore, an oxygen concentration difference occurred between the gas phase/melt interface and the melt/metal interface, forming an oxygen concentration cell and initiating electrochemical corrosion (seeing Fig. 12):

The anodic reaction (melt/metal interface):



The cathodic reaction (gas phase/melt interface):



Thus, in the molten salt, the combination of metal ions and O^{2-} occurred to form oxide particles.



As the corroded metal cations in the matrix/melt interface continued to accumulate and became excessive, Cl^{-} and SO_4^{2-} in the melt were attracted to migrate to the matrix/melt interface to maintain charge balance. This led to the enrichment of Cl^{-} or SO_4^{2-} near the matrix/melt interface (seeing Fig. 10b–d), and then two things happened.

First, metal chlorides were generated:



When these metal chlorides were mixed with alkali salts, new low-melting eutectic salts like $NaCl-FeCl_2$ could be formed [51], which increased the volume of the melt on the sample surface. As a result, the excess liquid phase overflowed from the sample surface, contaminating the inner walls of the porcelain boats, as shown in Fig. 2b–d. Furthermore, the dissolved metal chlorides diffused outward through the melt along the concentration gradient towards the gas phase/melt interface [52], along which path the oxygen partial pressure gradually increased, and thus different oxides were formed sequentially (Eq. (10)).

Likewise, in the corrosion tests at 510–580 °C, “active oxidation” was also always presented. Once the Cl_2 originated from reactions (2), (3), (6), (7), and (10) permeated to the matrix/melt interface, it facilitated the generation of metal chlorides and accelerated corrosion (seeing Fig. 11).

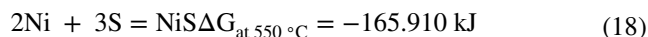
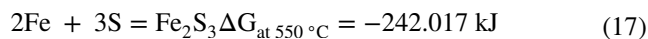
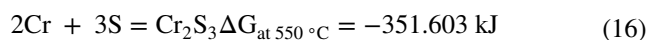
Second, the internal sulfidation reactions took place.

Specifically, SO_4^{2-} in the melt was consumed through the following reaction [53]:

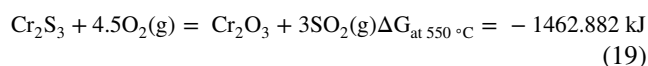


Thus, metal sulfides formed at the matrix/melt interface. Due to the thermodynamically more negative Gibbs free

energy for the formation of Cr sulfides compared to Fe and Ni sulfides, Cr sulfides were preferentially formed.



While sulfides could undergo oxidation to form oxides and SO_2 in the presence of O_2 , the sulfides located at the melt/matrix interface were difficult to be oxidized due to the limited O_2 in the melt near the surface of the matrix. Oxidation to metal oxides and SO_2 was only possible for the outer sulfides near the melt/gas phase interface. The SO_2 formed would escape into the atmosphere, which is why no S element was detected in the outer corrosion products.



In addition, in the melt, the O^{2-} decomposed in reaction (15) can also combine with metal ions to form metal oxides.



Reactions (16)–(20) result in the consumption of the three products generated in reaction (15), promoting the continuation of reaction (15) in the forward direction. This leads to the rapid reduction and depletion of SO_4^{2-} . Consequently, sulfate was not detected in the corrosion products upon completion of the test.

The difference in the content of S and Cl within the corrosion products arises from the fact that Cl_2 in the atmosphere can penetrate into the melt again and react with the metal to form metal chloride salts again. As a result, a large amount of Cl elements remains detectable within the corrosion products. On the contrary, when SO_2 in the atmosphere returns to the melt, it fails to induce the formation of metal sulfates due to the low partial pressure of O_2 within the melt.

In the late stage of corrosion (72–168 h), it is speculated that the salt on the surface of the metal sample at 550 and 580 °C was largely evaporated due to high temperatures, resulting in a large reduction of liquid-phase molten salt on the sample surfaces. Accordingly, the rapid migration and diffusion of ions lost their path, and the electrochemical reactions disappeared. Then the subsequent corrosion rate was limited by chemical reactions which were similar to those at 460 °C, so the corrosion rate exhibited a significant relative decrease. This result showed that at higher temperatures, the rapid evaporation of molten salts could also act to slow down corrosion. However, in the actual site, the salt substances in the MSWI flue gas will continuously deposit

on the heating surfaces, so the corrosion will not stop due to the evaporation of the salts.

In summary, compared with 460 °C, at 510–580 °C, under the joint influence of Cl^- and SO_4^{2-} , the main elements Fe and Cr in the 310S alloy were depleted at an accelerated rate, thus leaving metallic Ni at the edge of the matrix, which was consistent with previous research results [38].

The reason why NiO was not detected in the corrosion products at 460–580 °C (seeing Fig. 10) can be described as follows: i) The Gibbs free energy of forming NiCl_2 is much higher than those of FeCl_2 and CrCl_2 at 460–580 °C (as listed in Table 2), which means that it is relatively difficult for Ni element to be chlorinated into NiCl_2 [54]. ii) Compared with Cr and Fe elements, Ni element accounts for less in 310S alloy, so even if NiCl_2 was formed, its amount was very small. iii) A much higher O_2 partial pressure is required for the conversion of NiCl_2 to NiO, compared with that of CrCl_2 and FeCl_2 . Therefore, even if a small amount of NiCl_2 was generated at the matrix/scale interface with limited oxygen partial pressure, it was difficult to be preferentially oxidized [19].

Conclusion

In this work, the corrosion mechanism of 310S alloy deposited with NaCl/50 wt.% K_2SO_4 exposed to a typical MSWI flue gas atmosphere of 7 vol % O_2 + 600 ppm HCl + 100 ppm SO_2 + N_2 was studied. The effect of temperature on its corrosion behavior was also compared by testing at 460, 510, 550, and 580 °C. Through the measurement of macroscopic morphology and corrosion kinetics, as well as phase analysis of corrosion products by XRD and elemental analysis of cross-sections of corrosion products by SEM/EDS, a clear corrosion process was gradually revealed. The main conclusions can be drawn from this work, as follows: Under the test conditions employed in this study, 310S alloy suffered severe corrosion. NaCl/50 wt.% K_2SO_4 was an extremely corrosive agent. Corrosion became more severe as the temperature increased from 460 °C to 580 °C. The corrosion mechanism was different at various temperatures. At 460 °C, NaCl/50 wt.% K_2SO_4 did not melt and mostly remained in a solid state, and the precipitation of Fe_2O_3 , Fe_3O_4 , and Cr_2O_3 in the corrosion products was observed. The degradation of the metal in this case mainly came from the reactions between NaCl and the metal matrix, the consumption of the metal by chromate and ferrite, plus the “active oxidation” induced by HCl, SO_2 , and O_2 . At 510–580 °C, NaCl/50 wt.% K_2SO_4

has completely melted, forming a melt on the metal surface, and considerable metal chlorides and even metal sulfates were observed at the metal matrix/scale interface. In this case, the corrosion mechanism is mainly “electrochemistry” + “active oxidation”. The presence of a discrepancy in oxygen partial pressure between the melt/gas phase interface and the matrix/melt interface created an oxygen concentration battery that accelerated metal consumption at the melt/matrix interface. Therefore, under the combined action of Cl^- , SO_4^{2-} in the melt, and Cl_2 in the atmosphere, metal chlorides and metal sulfides were generated. Oxidation of these chlorides caused the metal to be consumed continuously until the molten salt evaporated away and then corrosion slowed down.

Acknowledgements This study was supported by the National Key Research and Development Program of China [Grant No. 2018YFC1901302], and the Innovative Research Groups of the National Natural Science Foundation of China [Grant No. 51621005].

Funding National Key Research and Development Program of China, 2018YFC1901302, Innovative Research Group Project of the National Natural Science Foundation of China, 51621005, Xuguang Jiang

References:

1. Wienchol P, Szlęk A, Ditaranto M (2020) Waste-to-energy technology integrated with carbon capture—challenges and opportunities. *Energy* 198:117352. <https://doi.org/10.1016/j.energy.2020.117352>
2. Moya D, Aldás C, López G, Kaparaju P (2017) Municipal solid waste as a valuable renewable energy resource: a worldwide opportunity of energy recovery by using waste-to-energy technologies. *Energy Procedia* 134:286–295. <https://doi.org/10.1016/j.egypro.2017.09.618>
3. Dong J, Tang Y, Nzihou A, Chi Y, Weiss-Hortala E, Ni M (2018) Life cycle assessment of pyrolysis, gasification and incineration waste-to-energy technologies: theoretical analysis and case study of commercial plants. *Sci Total Environ* 626:744–753. <https://doi.org/10.1016/j.scitotenv.2018.01.151>
4. Wang Y, Zhang X, Liao W, Wu J, Yang X, Shui W, Deng S, Zhang Y, Lin L, Xiao Y, Yu X, Peng H (2018) Investigating impact of waste reuse on the sustainability of municipal solid waste (MSW) incineration industry using emergy approach: A case study from Sichuan province. *China Waste Manage* 77:252–267. <https://doi.org/10.1016/j.wasman.2018.04.003>
5. Dastjerdi B, Strezov V, Kumar R, Behnia M (2019) An evaluation of the potential of waste to energy technologies for residual solid waste in new South Wales. *Australia Renewable and Sustainable Energy Reviews* 115:109398. <https://doi.org/10.1016/j.rser.2019.109398>
6. Viklund P, Hjärnhede A, Henderson P, Stålenheim A, Pettersson R (2013) Corrosion of superheater materials in a waste-to-energy

- plant. *Fuel Process Technol* 105:106–112. <https://doi.org/10.1016/j.fuproc.2011.06.017>
7. Otsuka N (2008) A thermodynamic approach on vapor-condensation of corrosive salts from flue gas on boiler tubes in waste incinerators. *Corros Sci* 50:1627–1636. <https://doi.org/10.1016/j.corsci.2008.02.004>
 8. Krumm L, Galetz MC (2018) Impact of deposits and their morphology on the active corrosion of iron in chlorine- and sulfur-containing atmospheres in the temperature range of 350–500 °C. *Oxid Met* 90:365–381. <https://doi.org/10.1007/s11085-018-9845-6>
 9. Reichelt J, Pfrang-Stotz G, Bergfeldt B, Seifert H, Knapp P (2013) Formation of deposits on the surfaces of superheaters and economisers of MSW incinerator plants. *Waste Manage* 33:43–51. <https://doi.org/10.1016/j.wasman.2012.08.011>
 10. Lindberg D, Becidan M, Sørum L (2010) High efficiency waste-to-energy plants—effect of ash deposit chemistry on corrosion at increased superheater temperatures. *Energy Fuel* 24:5387–5395. <https://doi.org/10.1021/ef100801e>
 11. Ma W, Wenga T, Frandsen FJ, Yan B, Chen G (2020) The fate of chlorine during MSW incineration: vaporization, transformation, deposition, corrosion and remedies. *Prog Energy Combust* 76:100789. <https://doi.org/10.1016/j.peccs.2019.100789>
 12. Dal Pozzo A, Muratori G, Antonioni G, Cozzani V (2021) Economic and environmental benefits by improved process control strategies in HCl removal from waste-to-energy flue gas. *Waste Manage* 125:303–315. <https://doi.org/10.1016/j.wasman.2021.02.059>
 13. Liu X, Duan Y, Chen Q, Long L, Lv G, Huang Q, Jiang X (2022) Study of corrosion kinetic measurement and morphology observation of superheater tube 12cr1mov alloy in simulated mswi flue gas containing varied HCl or SO₂ concentrations. *ACS Omega* 7:23929–23938. <https://doi.org/10.1021/acsomega.2c02722>
 14. Sadeghimeresht E, Reddy L, Hussain T, Huhtakangas M, Markocsan N, Joshi S (2018) Influence of KCl and HCl on high temperature corrosion of HVAF-sprayed NiCrAlY and NiCrMo coatings. *Mater Design* 148:17–29. <https://doi.org/10.1016/j.matdes.2018.03.048>
 15. Enestam S, Bankiewicz D, Tuiremo J, Mäkelä K, Hupa M (2013) Are NaCl and KCl equally corrosive on superheater materials of steam boilers? *Fuel* 104:294–306. <https://doi.org/10.1016/j.fuel.2012.07.020>
 16. Asteman H, Spiegel M (2007) Investigation of the HCl (g) attack on pre-oxidized pure Fe, Cr, Ni and commercial 304 steel at 400 °C. *Corros Sci* 49:3626–3637. <https://doi.org/10.1016/j.corsci.2007.03.028>
 17. Folkesson N, Johansson LG, Svensson JE (2007) Initial stages of the hcl-induced high-temperature corrosion of alloy 310. *J Electrochem Soc* 154:C515–C521. <https://doi.org/10.1149/1.2754174>
 18. Grabke HJ, Reese E, Spiegel M (1995) The effects of chlorides, hydrogen chloride, and sulfur dioxide in the oxidation of steels below deposits. *Corros Sci* 37:1023–1043. [https://doi.org/10.1016/0010-938X\(95\)00011-8](https://doi.org/10.1016/0010-938X(95)00011-8)
 19. Zahs A, Spiegel M, Grabke HJ (2000) Chloridation and oxidation of iron, chromium, nickel and their alloys in chloridizing and oxidizing atmospheres at 400–700°C. *Corros Sci* 42:1093–1122. [https://doi.org/10.1016/S0010-938X\(99\)00142-0](https://doi.org/10.1016/S0010-938X(99)00142-0)
 20. Dal Pozzo A, Lazazzara L, Antonioni G, Cozzani V (2020) Techno-economic performance of HCl and SO₂ removal in waste-to-energy plants by furnace direct sorbent injection. *J Hazard Mater* 394:122518. <https://doi.org/10.1016/j.jhazmat.2020.122518>
 21. Zhang H, Yu S, Shao L, He P (2019) Estimating source strengths of HCl and SO₂ emissions in the flue gas from waste incineration. *J Environ Sci* 75:370–377. <https://doi.org/10.1016/j.jes.2018.05.019>
 22. Wenga T, Chen G, Ma W, Yan B (2019) Study on corrosion kinetics of 310H in different simulated MSW combustion environment. The influence of SO₂ and H₂O on NaCl assisted corrosion. *Corros Sci* 154:254–267. <https://doi.org/10.1016/j.corsci.2019.04.013>
 23. Liu X, Chen Q, Long L, Meng X, Lv G, Huang Q, Jiang X (2021) In-situ sampling investigation of deposition and corrosion of convective heating surfaces in a grate type municipal solid waste incineration plant: a case study. *Waste Disposal & Sustainable Energy* 3:299–308. <https://doi.org/10.1007/s42768-021-00087-8>
 24. Zhao J, Wei X, Li T, Li H, Bin F (2018) Behavior of alkali metals in fly ash during waste heat recovery for municipal solid waste incineration. *Energy Fuel* 32:4417–4423. <https://doi.org/10.1021/acs.energyfuels.7b03001>
 25. Abu Warda N, López AJ, Pedraza F, Utrilla MV (2021) Corrosion behavior of T24, T92, VM12, and AISI 304 steels exposed to KCl-NaCl-K₂SO₄-Na₂SO₄ salt mixtures. *Mater Corros* 72:936–950. <https://doi.org/10.1002/maco.202012139>
 26. Karlsson S, Jonsson T, Hall J, Svensson J, Liske J (2014) Mitigation of fireside corrosion of stainless steel in power plants: a laboratory study of the influences of SO₂ and KCl on initial stages of corrosion. *Energy Fuel* 28:3102–3109. <https://doi.org/10.1021/ef402127h>
 27. Karlsson S, Pettersson J, Svensson JE, Johansson LG (2011) KCl-induced high temperature corrosion of the austenitic stainless steel 304L—the influence of SO₂. *Mater Sci Forum* 696:224–229. <https://doi.org/10.4028/www.scientific.net/MSF.696.224>
 28. Pettersson J, Pettersson C, Folkesson N, Johansson LG, Skog E, Svensson JE (2006) The influence of sulfur additions on the corrosive environments in a waste-fired CFB boiler. *Mater Sci Forum* 522–523:563–570. <https://doi.org/10.4028/www.scientific.net/MSF.522-523.563>
 29. Zhai W, Yang B, Zhang S, Ni J, Li S, Li Y (2020) Study on high temperature chlorination corrosion of metallic materials on the waste incineration boilers. *IOP Conference Series: Earth and Environmental Science* 450:12006. <https://doi.org/10.1088/1755-1315/450/1/012006>
 30. Li X, Liu Z, Li H, Wang Y, Li B (2013) Investigations on the behavior of laser cladding Ni-Cr-Mo alloy coating on TP347H stainless steel tube in HCl rich environment. *Surf Coat Technol* 232:627–639. <https://doi.org/10.1016/j.surfcoat.2013.06.048>
 31. Skrifvars BJ, Backman R, Hupa M, Salmenoja K, Vakkilainen E (2008) Corrosion of superheater steel materials under alkali salt deposits Part 1: The effect of salt deposit composition and temperature. *Corros Sci* 50:1274–1282. <https://doi.org/10.1016/j.corsci.2008.01.010>
 32. Bankiewicz D, Enestam S, Yrjas P, Hupa M (2013) Experimental studies of Zn and Pb induced high temperature corrosion of two commercial boiler steels. *Fuel Process Technol* 105:89–97. <https://doi.org/10.1016/j.fuproc.2011.12.017>
 33. Ma W, Wenga T, Zhang N, Chen G, Yan B, Zhou Z, Wu X (2017) Full-scale experimental investigation of deposition and corrosion of pre-protector and 3rd superheater in a waste incineration plant. *Sci Rep-Uk*. <https://doi.org/10.1038/s41598-017-17438-3>
 34. Verbinnen B, De Greef J, Van Caneghem J (2018) Theory and practice of corrosion related to ashes and deposits in a WtE boiler. *Waste Manage* 73:307–312. <https://doi.org/10.1016/j.wasman.2017.11.031>

35. Lee H, Yi S, Holsen TM, Seo Y, Choi E (2018) Estimation of CO₂ emissions from waste incinerators: comparison of three methods. *Waste Manage* 73:247–255. <https://doi.org/10.1016/j.wasman.2017.11.055>
36. Bal M, Siddiqi H, Mukherjee S, Meikap BC (2019) Design of self priming venturi scrubber for the simultaneous abatement of HCl gas and particulate matter from the flue gas. *Chem Eng Res Des* 150:311–319. <https://doi.org/10.1016/j.cherd.2019.08.005>
37. Krumm L, Galetz MC (2017) Chlorine attack of carbon steel between 350 and 500°C and its importance regarding corrosion in waste incineration. *Oxid Met* 87:757–766. <https://doi.org/10.1007/s11085-017-9749-x>
38. Andersson P, Norell M (2005) Field test of superheater corrosion in a CFB waste boiler: Part II—scale formation characteristics. *Mater Corros* 56:550–560. <https://doi.org/10.1002/maco.200403853>
39. Maj I, Kalisz S, Szymajda A, Łaska G, Gołombek K (2021) The influence of cow dung and mixed straw ashes on steel corrosion. *Renew Energ* 177:1198–1211. <https://doi.org/10.1016/j.renene.2021.06.019>
40. Sadeghimeresht E, Reddy L, Hussain T, Markocsan N, Joshi S (2018) Chlorine-induced high temperature corrosion of HVAF-sprayed Ni-based alumina and chromia forming coatings. *Corros Sci* 132:170–184. <https://doi.org/10.1016/j.corsci.2017.12.033>
41. Li YS, Spiegel M, Shimada S (2005) Corrosion behaviour of various model alloys with NaCl-KCl coating. *Mater Chem Phys* 93:217–223. <https://doi.org/10.1016/j.matchemphys.2005.03.015>
42. Pan TJ, Zeng CL, Niu Y (2007) Corrosion of three commercial steels under ZnCl₂-KCl deposits in a reducing atmosphere containing HCl and H₂S at 400–500°C. *Oxid Met* 67:107–127. <https://doi.org/10.1007/s11085-006-9047-5>
43. Meißner TM, Montero X, Fähsing D, Galetz MC (2020) Cr diffusion coatings on a ferritic-martensitic steel for corrosion protection in KCl-rich biomass co-firing environments. *Corros Sci* 164:108343. <https://doi.org/10.1016/j.corsci.2019.108343>
44. Ahila S, Iyer SR, Radhakrishnan VM (1993) Melting point determination of the K₂SO₄-NaCl system. *J Mater Sci Lett* 12:1733–1734. <https://doi.org/10.1007/BF00517594>
45. Tholence F, Norell M (2002) AES characterization of oxide grains formed on ductile cast irons in exhaust environments. *Surf Interface Anal* 34:535–539. <https://doi.org/10.1002/sia.1355>
46. Li YS, Niu Y, Spiegel M (2007) High temperature interaction of Al/Si-modified Fe-Cr alloys with KCl. *Corros Sci* 49:1799–1815. <https://doi.org/10.1016/j.corsci.2006.10.019>
47. Tsaor C, Rock JC, Wang C, Su Y (2005) The hot corrosion of 310 stainless steel with pre-coated NaCl/Na₂SO₄ mixtures at 750°C. *Mater Chem Phys* 89:445–453. <https://doi.org/10.1016/j.matchemphys.2004.10.002>
48. Aye KK, Zhang J, Young DJ (2020) Effect of hydrogen chloride on corrosion behaviour of Fe-Cr alloys in wet CO₂ gas at 650°C. *Oxid Met* 94:51–80. <https://doi.org/10.1007/s11085-020-09978-3>
49. Nimmervoll M, Schmid A, Mori G, Hönig S, Haubner R (2021) Surface sulphide formation on high-temperature corrosion resistant alloys in a H₂S-HCl-CO₂ mixed atmosphere. *Corros Sci* 181:109241. <https://doi.org/10.1016/j.corsci.2021.109241>
50. Uusitalo MA, Vuoristo PMJ, Mäntylä TA (2004) High temperature corrosion of coatings and boiler steels below chlorine-containing salt deposits. *Corros Sci* 46:1311–1331. <https://doi.org/10.1016/j.corsci.2003.09.026>
51. Robelin C, Chartrand P, Pelton AD (2004) Thermodynamic evaluation and optimization of the (NaCl+KCl+MgCl₂+CaCl₂+MnCl₂+FeCl₂+CoCl₂+NiCl₂) system. *J Chem Thermodyn* 36:809–828. <https://doi.org/10.1016/j.jct.2004.05.005>
52. Spiegel M (1999) Salt melt induced corrosion of metallic materials in waste incineration plants. *Mater Corros* 50:373–393. [https://doi.org/10.1002/\(SICI\)1521-4176\(199907\)50:7%3c373::AID-MACO373%3e3.0.CO;2-T](https://doi.org/10.1002/(SICI)1521-4176(199907)50:7%3c373::AID-MACO373%3e3.0.CO;2-T)
53. Yang X, Peng X, Wang F (2007) Hot corrosion of a novel electrodeposited Ni-6Cr-7Al nanocomposite under molten (0.9Na,0.1K)₂SO₄ at 900°C. *Scripta Mater* 56:891–894. <https://doi.org/10.1016/j.scriptamat.2007.01.035>
54. Zhang S, Li H, Jiang Z, Zhang B, Li Z, Wu J, Feng H, Zhu H, Duan F (2020) Chloride- and sulphate-induced hot corrosion mechanism of super austenitic stainless steel S31254 under dry gas environment. *Corros Sci* 163:108295. <https://doi.org/10.1016/j.corsci.2019.108295>

Publisher's Note Springer Nature remains neutral with regard to jurisdictional claims in published maps and institutional affiliations.

Springer Nature or its licensor (e.g. a society or other partner) holds exclusive rights to this article under a publishing agreement with the author(s) or other rightsholder(s); author self-archiving of the accepted manuscript version of this article is solely governed by the terms of such publishing agreement and applicable law.